Quantitative magnetic resonance and optical imaging biomarkers of melanoma metastatic potential

Lin Z. Li[a,1], Rong Zhou[a,1], He N. Xu[a], Lily Moon[b], Tuoxiu Zhong[b], Eun Ju Kim[a], Hui Qiao[a], Ravinder Reddy[c], Dennis Leeper[d], Britton Chance[b,2], and Jerry D. Glickson[a]

[a]Department of Radiology, School of Medicine, University of Pennsylvania, B6 Blockley Hall, 423 Guardian Drive, Philadelphia, PA 19104; [b]Johnson Research Foundation, Department of Biochemistry and Molecular Biophysics, School of Medicine, University of Pennsylvania, 250 Anatomy Chemistry Building, Philadelphia, PA 19104; [d]Division of Experimental Radiation Oncology, Department of Radiation Oncology, Kimmel Cancer Center, Thomas Jefferson University, Philadelphia, PA 19107; and [c]Metabolic Magnetic Resonance Research and Computing Center, B1 Stellar-Chance Laboratories, Department of Radiology, School of Medicine, University of Pennsylvania, Philadelphia, PA 19104

Contributed by Britton Chance, March 1, 2009 (sent for review August 25, 2008)

Noninvasive or minimally invasive prediction of tumor metastatic potential would facilitate individualized cancer management. Studies were performed on a panel of human melanoma xenografts that spanned the full range of metastatic potential measured by an in vivo lung colony assay and an in vitro membrane invasion culture system. Three imaging methods potentially transferable to the clinic [dynamic contrast-enhanced (DCE) MRI, $T_{1\rho}$-MRI, and low-temperature fluorescence imaging (measurable on biopsy specimens)] distinguished between relatively less metastatic and more metastatic human melanoma xenografts in nude mice. DCE-MRI, analyzed with the shutter-speed relaxometric algorithm and using an arterial input function simultaneously measured in the left ventricle of the mouse heart, yielded a blood transfer rate constant, K_{trans}, that measures vascular perfusion/permeability. K_{trans} was significantly higher in the core of the least metastatic melanoma (A375P) than in the core of the most metastatic melanoma (C8161). C8161 melanoma had more blood vascular structures but fewer functional blood vessels than A375P melanoma. The A375P melanoma exhibited mean $T_{1\rho}$ values that were significantly higher than those of C8161 melanoma. Measurements of T_1 and T_2 relaxation times did not differ significantly between these 2 melanomas. The mitochondrial redox ratio, Fp/(Fp + NADH), where Fp and NADH are the fluorescences of oxidized flavoproteins and reduced pyridine nucleotides, respectively, varied linearly with the in vitro invasive potential of the 5 melanoma cell lines (A375P, A375M, A375P10, A375P5, and C8161). This study shows that a harsh microenvironment may promote melanoma metastasis and provides potential biomarkers of metastatic potential.

dynamic contrast enhanced MRI | mitochondrial redox state | T1rho | invasive potential | human melanoma xenografts

Melanoma is treated primarily by surgical excision, which is often curative if the tumor is detected in its early stages. However, if recurrence with metastasis occurs, the prognosis is very poor because effective methods for treating systemic disease are not available. Evaluation of the metastatic potential of a melanoma at the time of surgery could determine the aggressiveness of the surgical procedures to be undertaken and the frequency of postsurgical surveillance.

Criteria currently available for staging human melanoma malignancies and predicting their metastatic potential include histopathological evaluation, height of the lesion, disease progression to sentinel lymph nodes, and genomic and proteomic approaches currently under development and evaluation (1–5). The objective of this study was to explore a variety of noninvasive and biopsy-based imaging methods that could be used to better distinguish between aggressive and indolent neoplasms and to identify biomarkers of tumor aggressiveness.

We chose to study melanoma because of the availability of a panel of human melanoma cell lines and their corresponding xenografts in immunosuppressed mice that span the full range of progression to metastasis. The invasive potential of 5 cell lines had been determined in vitro by measuring the fraction of melanoma cells that moved through a Matrigel barrier in a fixed time interval (24 h), falling in rank order, A375P (3%) < A375M (7%) < A375P10 (9.5%) < A375P5 (11%) < C8161 (13.5%) (E. Seftor, personal communication) (6, 7). The number of lung metastases had been measured in the mouse xenografts of these melanoma lines, falling in the rank order, A375P < A375P5 < A375P10 < A375M < C8161 (E. Seftor, personal communication) (6, 8, 9).

We evaluated 2 clinically applicable noninvasive MRI techniques [dynamic contrast enhancement (DCE)-MRI and $T_{1\rho}$-MRI] as potential biomarkers of tumor metastatic potential. DCE-MRI was chosen because differences in blood flow and/or permeability between indolent and aggressive tumors were anticipated (10), whereas $T_{1\rho}$-MRI was used because it is sensitive to the interaction of water molecules with macromolecules (11–15). We compared these methods with conventional T_1- and T_2-MRI methods. Because tumor metastasis or cellular motility may be related to the bioenergetic state of the tumor and hence to mitochondrial metabolism, we also evaluated low-temperature NADH/flavoprotein (Fp) surface fluorescence imaging or "redox scanning" (16), which can be clinically implemented on biopsy specimens. We initially compared only the most aggressive melanoma (C8161) with the most indolent melanoma (A375P) by DCE-MRI, $T_{1\rho}$-MRI, and redox scanning. To examine trends in the measured properties of these melanomas, we later added a melanoma model of intermediate metastatic potential (A375M) to the $T_{1\rho}$ measurements and examined the optical properties of the entire panel of melanomas. Preliminary results were reported and published in the conference proceedings of the International Society of Oxygen Transport to Tissues (17, 18).

Results

We have indentified significant correlations between the measured values of K_{trans}, $T_{1\rho}$, and mitochondrial redox ratios with the aggressiveness of these melanomas (see Table S1 for tumor number and size for each imaging study). The data also showed significant differences between the tumor core and rim regions in the DCE-MRI and redox imaging measurements. The tumor core in redox imaging is defined as the more oxidized region with higher redox ratio and the rim as the more reduced region surrounding the core. The tumor core for DCE-MRI was defined arbitrarily as covering one-third of the radius from the

Author contributions: L.Z.L., R.Z., T.Z., R.R., D.L., B.C., and J.D.G. designed research; L.Z.L., R.Z., H.N.X., L.M., T.Z., E.J.K., and H.Q. performed research; L.Z.L., R.Z., H.N.X., L.M., T.Z., E.J.K., H.Q., R.R., D.L., B.C., and J.D.G. analyzed data; and L.Z.L., R.Z., H.N.X., H.Q., D.L., B.C., and J.D.G. wrote the paper.

The authors declare no conflict of interest.

[1]L.Z.L. and R.Z. contributed equally to this work.

[2]To whom correspondence should be addressed. E-mail: chance@mail.med.upenn.edu.

This article contains supporting information online at www.pnas.org/cgi/content/full/0901807106/DCSupplemental.

www.pnas.org/cgi/doi/10.1073/pnas.0901807106

Table 1. Parameters determined by fitting the melanoma DCE-MRI data to the FXL and FXR models

Model	Parameter	Tumor core		Tumor rim	
		C8161 ($n = 3$)	A375P ($n = 4$)	C8161 ($n = 3$)	A375P ($n = 4$)
FXL	K_{trans}, min^{-1}	0.07 ± 0.00	0.09 ± 0.02	0.12 ± 0.01	0.16 ± 0.05
	ν_e	0.17 ± 0.12	0.22 ± 0.01	0.35 ± 0.23	0.26 ± 0.01
FXR	K_{trans}, min^{-1}	0.07 ± 0.00*,**	0.17 ± 0.01*	0.19 ± 0.04**	0.38 ± 0.18
	ν_e	0.18 ± 0.12	0.35 ± 0.04	0.45 ± 0.28	0.40 ± 0.07
	τ_i, s	0.4 ± 0.4	2.1 ± 1.7	1.8 ± 0.2	1.8 ± 0.4

The data indicate the FXR model can detect a significant difference in K_{trans} in the tumor core between the most metastatic C8161 and the least metastatic A375P melanomas (*, $P < 0.05$, t test), whereas the FXL model cannot. Statistical differences (**, $P < 0.05$, t test) between the tumor core and rim were detected for the C8161 melanoma but not for the A375P melanoma.

core to the outer boundary of the tumor and the tumor rim as the region enhanced in postcontrast images (see more details in *Materials and Methods*). Tumor core and rim were not defined for $T_{1\rho}$-MRI experiments. Note that no coregistration was used among any imaging modalities (DCE-MRI, $T_{1\rho}$-MRI, redox imaging) nor between images and tumor histology.

K_{trans} in Tumor Core Distinguishes Between Highly Metastatic and Least Metastatic Melanomas. DCE-MRI studies were conducted on 2 types of melanoma xenografts, the most metastatic C8161 ($n = 3$) and the least metastatic (most indolent) A375P ($n = 4$). Table 1 presents the analysis by using 2 models: (*i*) the fast exchange limit (FXL)-constrained model that assumes that transcytolemmal water exchange is always infinitely fast relative to the longitudinal relaxation rate (i.e., the FXL always applies), and (*ii*) the fast exchange regime (FXR)-permitted model that allows for deviations from the FXL to a slower FXR that applies when the concentrations of paramagnetic contrast agents are high. The arterial input function (AIF), the time course of the gadolinium concentration in the blood, was determined by gated cardiac imaging of the left ventricle (19, 20). The FXL-constrained model measures K_{trans} and extracellular volume fraction (ν_e), whereas the FXR-permitted model measures the same parameters plus the mean lifetime of intracellular water (τ_i). Statistically significant parameter differences were obtained only from the FXR-permitted model for K_{trans} in the core of the aggressive C8161 melanoma vs. the core of the indolent A375P melanoma and for K_{trans} in the core vs. the rim of the aggressive C8161 melanoma. In the FXR-permitted model, K_{trans} in the tumor core was about twice as great in the indolent A375P melanoma as in the aggressive C8161 melanoma (t test; $P < 0.05$).

$T_{1\rho}$ Distinguishes Between Highly Metastatic and less Metastatic Melanomas, Whereas T_1 and T_2 Do Not. $T_{1\rho}$-MRI was performed on mouse xenografts of 3 melanoma lines with the following rank order of aggressiveness: A375P < A375M < C8161. Significant differences were observed between the average $T_{1\rho}$ values of the indolent A375P and the most aggressive C8161 melanomas at spin-locking frequencies (SLFs) ranging from 490 to 4,000 Hz. Fig. 1 plots mean $T_{1\rho}$ values vs. SLFs for 4 A375P tumors (mean volume = 0.50 ± 0.18 cm^3) and 5 C8161 tumors (mean volume = 0.49 ± 0.38 cm^3). When the SLF was >800 Hz, $T_{1\rho}$ tended to increase with SLF, and the indolent melanoma exhibited distinctly longer relaxation times than the aggressive melanoma. When the SLF was <800 Hz, the separation of data points from the 2 melanoma types was smaller but still apparent, although some of the data points overlapped. Linear regression was performed on the $T_{1\rho}$ dispersion data for each tumor type. No statistically significant difference was found for the mean slopes of the A375P and C8161 melanomas. However, the mean intercept (98 ± 14 vs. 76 ± 11 s) exhibited a statistically significant difference between these 2 xenografts ($P = 0.042$). The average T_1 and T_2 values (54 ± 9 ms for the least metastatic A375P melanoma and 45 ± 8 ms for the most metastatic C8161 melanoma) were not significantly different on the basis of t tests ($P > 0.05$) (Table S2). Therefore, only the $T_{1\rho}$ relaxation time was suitable for distinguishing between the most and least metastatic melanomas.

We then performed $T_{1\rho}$-MRI studies of A375M melanomas, whose aggressiveness falls between the indolent A375P melanoma and the most aggressive C8161 melanoma ($n = 4$, mean volume = 0.45 ± 0.2 mm^3). The average $T_{1\rho}$ values (when SLF was ≈2,000 Hz) for each type of melanoma were 117 ± 14, 97 ± 3, and 88 ± 5 ms for A375P, A375M, and C8161, respectively. ANOVA indicated a significant difference among the 3 melanoma types for $T_{1\rho}$ ($P = 0.002$), but not for T_2 ($P = 0.25$) or for tumor volume ($P = 0.96$) (Table S2). The mean $T_{1\rho}$ value for the A375P and A375M melanomas was higher than that of the C8161 melanoma ($P = 0.02$, t test). The mean $T_{1\rho}$ value for the A375P melanoma was higher than for the A375M melanoma but with borderline statistical significance ($P = 0.06$, t test). The corresponding mean transverse relaxation rates ($1/T_{1\rho}$) of these 3 melanoma types (8.5 ± 1.0 s^{-1} for A375P, 10.3 ± 0.3 s^{-1} for A375M, and 11.3 ± 0.6 s^{-1} for C8161) exhibited a trend toward increasing linearly with the invasive potential of the corresponding tumor lines (3%, 7% and 13.5%, respectively), but this trend did not reach statistical significance ($R^2 = 0.92$; $P = 0.18$) (Fig. 2).

Mitochondrial Redox Ratio Correlates with the Invasive Potential of 5 Melanoma Xenografts. We conducted redox scanning on xenografts of all 5 melanoma cell lines spanning the full range of

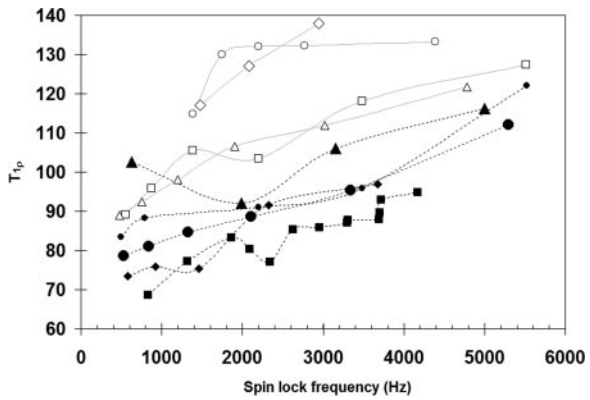

Fig. 1. Mean $T_{1\rho}$ values versus the SPF for the least metastatic A375P melanoma (open symbols, $n = 4$) and the most metastatic C8161 melanoma (solid symbols, $n = 5$). Each group of symbols (open and solid) of different shapes represents 1 mouse. The average intercept 98 ± 14 s from linear regressions for each A375P tumor differs significantly from that of the C8161 melanoma (76 ± 11 s) (t test, $P = 0.04$).

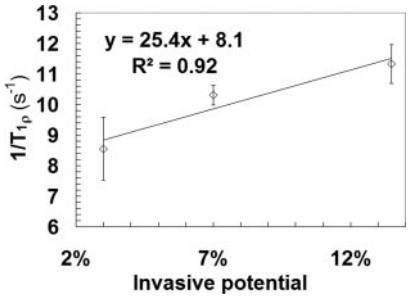

Fig. 2. The relaxation rates ($1/T_{1\rho}$) of A375P, A375M, and C8161 melanomas increase linearly with the invasive potentials of the corresponding cell lines measured in vitro in a Boyden chamber (A375P < A375M < C8161). Linear regression, $R^2 = 0.92$, $P = 0.18$.

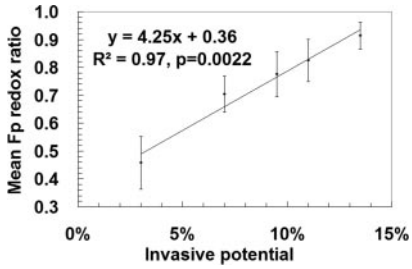

Fig. 4. Correlation of the mean Fp redox ratios with the invasive potentials of 5 melanoma lines measured by the Boyden chamber method. The mean Fp redox ratios were averaged in the oxidized tumor areas across all tumor sections (total number of sections 12–29) pooled together from 3–5 tumors for each xenograft line. Linear regression, $R^2 = 0.97$, $P = 0.002$.

invasive potential. The Fp redox ratio proved capable of distinguishing between these 5 melanoma lines. Fig. 3 shows representative Fp redox ratio images and corresponding histograms for a typical tissue section of each melanoma line. The tumors from the indolent A375P melanoma exhibited a nearly homogeneous low Fp redox ratio within the entire tumor. There were small regions with relatively high Fp redox ratios, which accounts for the right tail end of the histogram in Fig. 3*E*.

All of the other more metastatic tumor lines exhibited 2 distinct peaks in the Fp redox ratio histograms. The right peak with higher Fp redox ratios corresponded to the more oxidized tumor core, whereas the left peak with lower Fp redox ratios corresponded to the tumor rim that was relatively more reduced in mitochondrial redox state. The right peak values of Fp redox ratios were averaged across multiple imaging sections and different tumors, i.e., 2–9 imaging sections for each tumor, 3–5 tumors and 12–29 imaging sections in total for each melanoma xenograft line. For the most indolent A375P melanoma with only 1 major peak in the histogram, the mean value was estimated from the redox ratios corresponding to the shoulder on the right side of the peak.

ANOVA indicated that the mean Fp redox ratio in the oxidized region distinguished between these 5 melanoma lines ($P = 7 \times 10^{-8}$), but there was no significant difference in average tumor volume among these lines ($P = 0.7$). The most aggressive C8161 melanoma had the most oxidized tumor cores with mean Fp redox ratios across tissue sections (0.91 ± 0.05) significantly higher than those of other less aggressive melanomas (A375P, 0.46 ± 0.09; A375M, 0.70 ± 0.07; A375P10, 0.78 ± 0.08; A375P5, 0.83 ± 0.08; 2-tailed t test; $P < 0.002$). Statistically significant differences ($P < 0.01$) were found between any of the other 2 melanoma lines as well, except $P = 0.1$ between the A375P5 and A375P10 melanomas. An excellent correlation ($R^2 = 0.97$; $P = 0.002$) was obtained between the mean Fp redox ratios of the high Fp regions and the invasive potentials of all of the melanoma lines (Fig. 4). The global averages of Fp redox ratios across whole tumor sections correlated less consistently and with lower statistical significance with the invasive potentials across the 5 lines ($R^2 = 0.63$, $P = 0.1$).

Histology. Quantification of tumor microvasculature density (MVD) was obtained by immunohistological staining of CD31, an endothelial marker. The patency of microvasculature was obtained by the quantification of the percentage of tumor area that emitted blue fluorescence of Hoechst 33342 after i.v. injection of the Hoechst dye. A significantly higher MVD was observed in the rim of the most aggressive C8161 melanoma compared with the rim of the most indolent A375P melanoma ($P < 0.05$; Table S3), suggesting that the aggressive C8161 melanoma was more active in angiogenesis. In contrast, Hoechst dye measurements indicate that the indolent A375P melanoma has a higher level of patency than the aggressive C8161 mela-

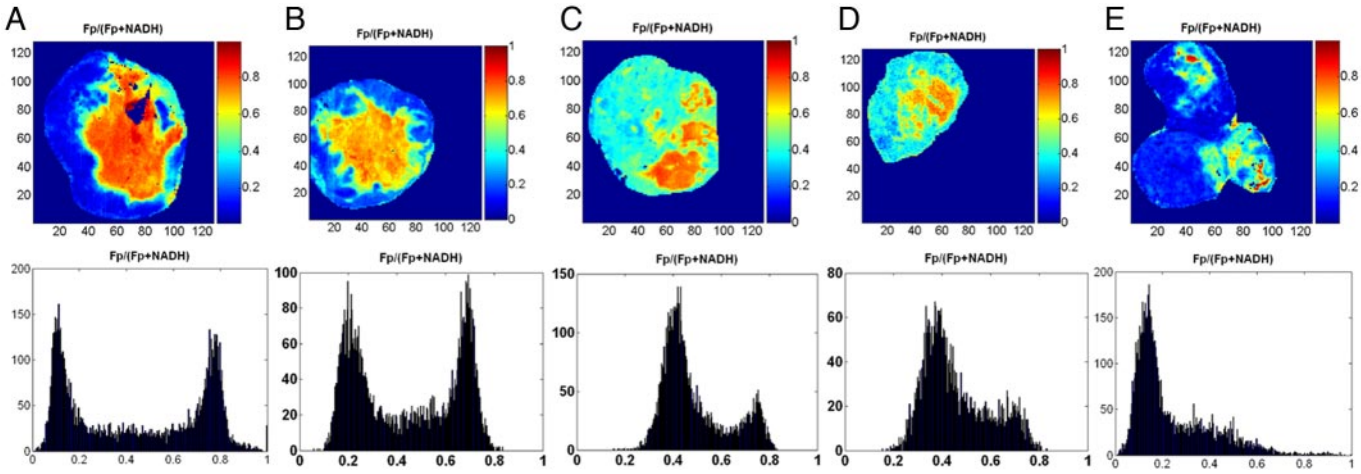

Fig. 3. Typical melanoma Fp redox ratio images and corresponding histograms: C8161 (*A*), A375P5 (*B*), A375P10 (*C*), A375M (*D*), and A375P (*E*) , following the decreasing rank of invasive potential in vitro. Distinct differences were detected between the tumor cores and rims for all aggressive melanomas (*A–D*). The tumor cores were more oxidized with higher redox ratios than the rims. This is also evident in the bimodal distribution of the histograms showing the number of image pixels (*y* axis) for specific redox ratios (*x* axis). The least metastatic A375P melanoma is largely reduced with a single histogram peak of a relatively low redox ratio. *A* and *E* and their corresponding histograms were duplicated from ref. 17. [Reproduced with permission from ref. 17 (Copyright 2007, Springer).]

noma with a statistical significant difference in the tumor rim ($P < 0.05$) and a borderline difference in the tumor core ($P = 0.07$) (Table S3).

Discussion

This study provides a model for identification of potential biomarkers of metastatic potential that could be tested in the clinic for melanoma, breast, prostate, and other types of cancers. We have identified 3 clinically translatable imaging methods to detect metastatic potential, DCE-MRI, $T_{1\rho}$-MRI, and NADH/Fp fluorescence imaging (redox scanning), and excluded 2 others (T_1- and T_2-MRI). By using a more realistic 2-compartment FXR-permitted or shutter-speed model first developed by Springer's laboratory (19, 21–25) that allows for deviations from the FXL for cell membrane water exchange, our DCE-MRI data demonstrated a clear difference in K_{trans} values at the tumor core between the most metastatic C8161 and indolent A375P melanomas. The most commonly used model (FXL) (26, 27) for kinetic modeling of DCE-MRI data failed to yield statistical significance for the differences in K_{trans}. We have also simultaneously measured the AIF in the mice whose tumor enhancement was monitored (19, 20); determination of the AIF is essential for evaluating the various models for analysis of DCE data.

Our $T_{1\rho}$-MRI data from 3 types of melanomas (A375P, A375M, and C8161) showed that $T_{1\rho}$ can differentiate significantly between the most metastatic (C8161) and the least metastatic (A375P) xenografts and $T_{1\rho}$ decreases with increasing in vivo metastatic potentials of these melanomas (based on lung colony assays). There was a trend toward linear correlation ($R^2 > 0.90$) of $1/T_{1\rho}$, with the invasive potential of these melanomas, although more measurements may be needed to establish a statistically significant difference between A375P and A375M melanomas. $T_{1\rho}$ may be subject to the influence of multiple factors in tissue physiological environments such as water content, macromolecular concentrations, pH and pO_2 (11, 13, 15, 28, 29). The mechanism producing the differences in $T_{1\rho}$ of tumors with different metastatic potential is still not well defined. Our data show that $T_{1\rho}$ differentiates highly metastatic melanomas from less metastatic ones, whereas T_1 and T_2 do not.

This study used redox imaging to evaluate tumor metastatic potential. We have chosen redox scanning for this study rather than conventional microscopy of frozen tissue sections because: (*i*) live tissue snap-frozen in liquid nitrogen will maintain the same metabolic status as in vivo; (*ii*) fluorescence signals of NADH under the low temperature of liquid nitrogen are ≈10-fold stronger than under room temperature (30); and (*iii*) measurement of the relative NADH and Fp fluorescence signal ratio has the advantages of being independent of the density of mitochondria, avoiding interference from other fluorophores and demanding less stringent instrumentation. More importantly, the redox ratio measurement provides an index of steady-state mitochondrial metabolism. Our data have shown a highly significant linear correlation of the Fp redox ratio in the tumor core with the invasive potential of 5 types of melanomas spanning the full range of tumor progression to metastasis. Compared with other imaging biomarkers that may only provide binary differentiation of malignant from benign or indolent tumors, the continuously quantitative "scaling" of tumors aggressiveness on the basis of the redox ratio is expected to facilitate personalized clinical cancer management.

Implications on the Relationship of Melanoma Microenvironment to Metastatic Potential. In general, tumor microenvironment, cancer cell survivability, and their metastatic potential are closely linked. A harsh microenvironment exhibiting characteristics such as hypoxia, acidosis, ischemia, nutritional deprivation, or cytotoxic effect of radiation therapy or chemotherapy is known to promote tumor malignancy and metastasis (31–35). Our data provide quantitative assessment of the relationship between melanoma microenvironment and metastatic potential.

Nutrient supply to tumor core. More aggressive tumors might be expected to require more blood vessels because of the need to transport nutrients to tumors for growth and proliferation. However, the DCE-MRI data show that the most metastatic C8161 melanoma has lower blood transfer rate constants K_{trans} in the tumor core than the least metastatic A375P melanoma. The parameter K_{trans} measures both vascular perfusion and the product of vascular permeability and surface area. However, because tumors tend to have highly leaky vasculature, it is likely that small paramagnetic contrast agents such as gadolinium chelates are in the perfusion-limited state and K_{trans} predominantly measures tumor perfusion. In general, DCE-MRI results are in good agreement with the immunohistochemistry of tumor vasculature. A significant difference between the rim and core of the aggressive C8161 melanoma obtained from Hoechst dye patency measurements ($P < 0.05$; Table S3) is consistent with the difference in K_{trans} values of the 2 compartments. Likewise, the higher K_{trans} of the core of the least metastatic A375P melanoma compared with that of the most metastatic C8161 melanoma is supported by Hoechst dye patency results, which revealed that the positive staining in the core of the A375P melanoma was ≈4 times that of the core of C8161 melanoma ($P = 0.07$; Table S3). Therefore, although the aggressive melanoma may produce more blood vasculature in the tumor core, it has less blood vessel patency and thus appears to be more poorly perfused with an overall decrease in functional blood exchange, i.e., lower K_{trans}. Limited blood perfusion has the dual effect of leading to oxygen and substrate deprivation. The latter appears more significant and is consistent with the more oxidized mitochondrial redox state observed in the most metastatic C8161 melanoma detected by redox imaging compared with that of the least metastatic A375P melanoma (see next section).

Mitochondrial redox state. In recent years, mitochondria and mitochondrial metabolism have received increased research interest because of their roles in many aspects of tumorigenesis, including mutagenesis, maintenance of the malignant phenotype, and control of apoptosis (36). Mitochondria have also been proposed as possible biomarkers of tumor malignancy and targets for therapy (37). Using redox imaging, this study probes the connection between tumor aggressiveness and mitochondrial redox state. We find that the redox state of mitochondrial flavoproteins (Fps) and pyridine nucleotides (NADH) reflects tumor aggressiveness and that a more oxidized state indicates increased aggressiveness and vice versa. A number of distinct mitochondrial respiratory states can be distinguished on the basis of Fp, NADH, and the redox ratio, i.e., either Fp redox ratio (Fp/(Fp + NADH) or NADH redox ratio (NADH/(Fp + NADH) (30, 38, 39). State 1 corresponds to adequate oxygen and low levels of ADP and endogeneous substrate. This condition is indicative of low levels of oxidative metabolism accompanied by high NADH and low Fp, i.e., low Fp redox ratio. In state 2 mitochondria are starved of substrate but have adequate oxygen and ADP; this state characteristically exhibits very high levels of Fp and low levels of NADH, i.e., high Fp redox ratio. State 3, which corresponds to adequate levels of oxygen, ADP, and substrate and, hence, high levels of oxidative metabolism, is also accompanied by a higher Fp redox ratio, but not as high as state 2, and lower NADH, but not as low as state 2. State 4 exhibits low mitochondrial respiratory activity with low ADP levels but with adequate supplies of substrate. This state exhibits a high NADH redox ratio but a low Fp redox ratio. State 5 corresponds to an anaerobic condition when oxygen is exhausted with high levels of ADP and substrate. Mitochondria are fully reduced in this state with the highest NADH and a higher NADH redox ratio than in state 4. Because the DCE-MRI data indicate lower functional blood exchange (perfusion/permeability) in the tumor core of the most

metastatic C8161 melanoma, the observation that the cores of the C8161 melanoma exhibit a significantly higher Fp redox ratio than the rims of these melanoma or the entire indolent A375P melanoma indicates that mitochondria in the cores of the aggressive melanoma are probably substrate-starved (state 2) rather than metabolically active and well-supplied with substrates (state 3), and that the rates of electron transport and ATP synthesis are low in the nutrient/oxygen-limited tumor cores. Histology with H&E staining (18) also indicates that melanoma cells in the core of an aggressive melanoma are morphologically different from cells in the rim, which are amply supplied with nutrients and oxygen. To date only a limited number of studies have indirectly implied a connection between the redox state (or NADH level) and the metastatic potential of tumors (40). More studies are needed to understand exactly how the mitochondrial redox ratio may be linked to the enhanced metastatic potential of melanomas.

Correlation of harsh tumor microenvironment with metastatic potential. Although our conclusions require verification in smaller tumors (volume <0.1 cm^3) to definitively exclude the effect of tumor body burden, we tentatively attributed the characteristics of these tumors to poor perfusion and state 2 mitochondrial metabolism in the absence of frank necrosis. Our histology results further indicated existence of intact cell bodies and low TUNEL-positive rate in the tumor core of more aggressive A375M and C8161 melanomass (18). The evidence supports the existence of viable cells in the tumor core and indicates that the more metastatic melanomas contain viable cancer cells in their cores, even under starvation conditions. The inhospitable environment may promote cancer cell metastasis. Previous studies have shown that hypoxia and acidosis promote tumor progression and metastasis by affecting the stability of chromosomes (33, 34, 41, 42). A poorly perfused core in the aggressive tumor would be expected to secrete VEGF and other cytokines that could facilitate metastasis. Our data indicate that a more inhospitable state in the cores of aggressive melanomas correlates with a higher potential for metastasis, i.e., it favors the survival of cells with the ability to migrate to a more favorable environment.

Materials and Methods

Animal Models and Evaluation of Invasiveness. The C8161 line (43) was established from a patient with a highly metastatic melanoma, and the A375P line (9) was from another patient with an indolent primary melanoma. The A375M was obtained from lung metastasis of an A375P melanoma in a mouse model (9). The metastatic potentials of A375P, A375M, and C8161 have been evaluated by counting the number of spontaneous metastases in lungs in mice with s.c. implanted xenografts of these tumor lines (8, 9). The C8161 line was the most metastatic, and the A375P line was the most indolent (barely metastatic in mouse models). The A375P5 and A375P10 lines were derived from A375P cells that migrated through reconstituted basal membranes for 5 and 10 passages, respectively. Animal model studies have shown that these 2 lines can form more lung microcolonies in mice than the primary cell line A375P after injection into the tail vein (E. Seftor, personal communication) (6).

Melanoma animal model protocols were approved by the Institutional Animal Care and Use Committee at the University of Pennsylvania. Human melanoma cells were grown in RPMI 1640 medium supplemented with 10% FBS and 20 mM Hepes solution. Melanoma cells (2×10^6) were s.c. implanted on the back shoulders or the thighs of 7- to 9-week-old male athymic nude mice (NCr-nu/nu; 20–35 g) obtained from the National Cancer Institute. After 1–2 months, the mice were examined by MRI and/or then killed for redox imaging by snap-freezing anesthetized mice with liquid nitrogen. The mean volumes of tumors and the number of tumors for each study have been compiled in Table S1. The tumor volume was calculated by $V = \pi/6 \times (L \times W \times H)$, where L, W, and H stand for the length, width, and height of the tumor measured by vernier calipers. At the time of the experiments, the tumor volumes ranged from $\approx$0.1 to 1 cm^3 (diameter of 6–13 mm) for all xenografts.

MRI. MR images were obtained either with commercial or home-built birdcage 50- or 30-mm ^{1}H coils in a Varian ANOVA spectrometer interfaced to a 4.7-T horizontal bore magnet equipped with a 12-cm gradient insert capable of generating magnetic field gradients of 25 G/cm. Mice were examined under anesthesia with the body core temperature at $\approx$37 °C, maintained by warm air flow (1% isofluorane, 100% O_2, flow rate 0.8 L/min) into the magnet bore. The mouse core temperature and heart rate were monitored in real time by a rectal temperature probe and ECG leads inserted s.c. into the limbs.

DCE-MRI of melanoma xenografts in vivo. DCE-MRI measurements at a rate of $\approx$2 s per image were performed as described (19, 20). The average signal intensities of DCE images in the tumor core and rim were modeled by using Springer's BOLus Enhanced Relaxation Overview (BOLERO) or shutter-speed method (19, 23), with the tumor core and rim defined as follows (see Fig. S1): Serial MRI images (2 s per image, $\approx$60 images) before and after injection of the contrast agent gadodiamide (Omniscan) were displayed. The peripheral region of the tumor that enhanced within 2 min postinjection was defined as the tumor rim. The central portion of the tumor covering one-third of the radius was defined as the tumor core.

MR $T_{1\rho}$-weighted imaging of melanoma xenografts. $T_{1\rho}$-weighted imaging pulse sequences used a fast spin-echo sequence as described by Reddy and colleagues (44, 45), with the following parameters: time of repetition (TR) 1 s, echo spacing 6 ms, matrix 128 $\times$ 128, field of view (FOV) 30–40 mm, slice thickness 2 mm, number of excitations 2, 6 times of spin locking (TSL) 16–125 ms; SLF 300–6,000 Hz. By fitting the signal as an exponential function of TSL, i.e., $\exp[-\mathrm{TSL}/T_{1\rho}]$, $T_{1\rho}$ was determined for every image pixel at a specific SLF. The mean value of $T_{1\rho}$ was also obtained by fitting the average signal values in a whole tumor section.

T_1-, T_2-weighted imaging. An inversion-recovery pulse sequence was used to quantify T_1 of arterial blood and tumor tissues as described (19). The T_2-weighted images were acquired with a conventional spin-echo sequence with TR 500 ms and 6 times of echo (TE) varying from 12 to 62 ms. Values of T_2 were determined by fitting the T_2-weighted imaging signal intensity to the exponential function, $\exp[-\mathrm{TE}/T_2]$.

Redox Scanning. Redox scanning of snap-frozen tissues in liquid nitrogen was performed as described by Quistorff et al. (16) with the following parameters: Fp excitation 440 nm (bandwidth 20 nm), emission 520 nm (bandwidth 40 nm); NADH excitation 365 nm (bandwidth 25 nm), emission 455 nm (bandwidth 70 nm), matrix 128 $\times$ 128, 80-μm in-plane resolution, and a light penetration depth of $\approx$10 μm because of ice crystal formation. The depths of the tissue sections were recorded as the thickness of tissues that were ground away. Data were analyzed with Matlab to obtain images of Fp redox ratios, i.e., Fp/(Fp + NADH) and the corresponding histograms. The x axis of a histogram represents the Fp redox ratio, and the y axis represents the number of image pixels having a specific redox ratio. For aggressive melanomas, the tumor core was defined as the more oxidized region with higher Fp redox ratios corresponding to the right peak in the histograms and the tumor rim corresponding to the left peak with lower Fp redox ratios.

Histology. To evaluate the vascular patency and microvascular density (MVD), 150 μL of 2% Hoechst-33342 (Sigma–Aldrich) was administered i.v. 1 min before tumor excision (see Table S1 for number of tumors used in such studies). The tumor was then embedded in OCT and 10-μm cryosections were obtained and stained with anti-mouse CD31 antibodies (BD Biosciences). To quantify the Hoechst dye staining, microscopic images (2$\times$) were obtained at 1 section per level and 3 levels per tumor, 3–6 FOV per level to cover the tumor rim region and 1 FOV to cover the core region (0.5 mm along the radius from the center of the section). The images were then imported into ImageJ software (version 1.38x; National Institutes of Health, Bethesda), which estimated the area emitting blue fluorescence versus the area of tumor in the same FOV. Percentage tumor areas that were positive for Hoechst dye were averaged over the rim and core region of each tumor. To estimate MVD, microscopic images (10$\times$) were obtained from the rim (3–6 FOV depending on tumor size) and core region (1–2 FOV) of the tumor; CD31 positive ''hot'' spots were counted in each FOV and converted to the number of vessels per mm^2 in the rim and core region of each tumor.

Statistical Analysis. ANOVA was performed to test for statistically significant differences between the measurements of a parameter (e.g., $T_{1\rho}$, T_2, tumor volume, redox ratio) among $>$2 groups of melanomas. A t test (2-tailed, unpaired with unequal variance) was then conducted to compare the difference between each of the group pairs. The t test was also used for evaluating the statistical significance of the difference of DCE-MRI observations between A375P and C8161 melanomas. Linear regression analysis was used to obtain the correlation coefficients and probability of significance for the plots in Figs. 2 and 4.

ACKNOWLEDGMENTS. We thank Drs. Mary Hendrix and Elisabeth Seftor for valuable discussions about melanoma metastasis models; Drs. Ravinder Regatte and Steven Pickup for assistance with the $T_{1\rho}$-weighted MRI measurements; Mr. Huaqing Zhao at the Westat Biostatistics and Data Management Core of the Children's Hospital of Philadelphia for assistance with statistical analysis; Drs. Thies Schroeder and Mark Dewhirst at Duke University for the protocol for Hoechst 33342 perfusion of tumors; and Mr. David Nelson for assistance in the preparation of the animal models and the manuscript. Melanoma cell lines and corresponding data of their in vitro invasive potential were obtained from the laboratory of Dr. Mary J. C. Hendrix (National Institutes of Health Grant CA 59702) at the Children's Memorial Research Center, Feinberg School of Medicine, Northwestern University, Chicago. This work was supported by National Institutes of Health Grants P01-CA56690-09A2 (to D.B.L. and J.D.G.), P50-CA 093372 (to M. Herlyn), R01-HL081185 (to R.Z.), and UO1-CA105490 (to L. A. Chodosh); Penn Network of Translational Research in Optical Imaging Grant U54-CA105008 (to Wafik El-Deiry); National Institutes of Health-supported Research Resource Grant P41-RR002305 (to R.R.); and a pilot grant from the University Research Foundation at the University of Pennsylvania (to L.Z.L.).

1. Gershenwald JE, et al. (1999) Multi-institutional melanoma lymphatic mapping experience: The prognostic value of sentinel lymph node status in 612 stage I or II melanoma patients. *J Clin Oncol* 17:976–983.
2. Balch CM, et al. (2001) Final version of the American Joint Committee on Cancer staging system for cutaneous melanoma. *J Clin Oncol* 19:3635–3648.
3. Balch CM, et al. (2001) Prognostic factors analysis of 17,600 melanoma patients: Validation of the American Joint Committee on Cancer melanoma staging system [see comment]. *J Clin Oncol* 19:3622–3634.
4. Thompson JF, Shaw HM, Hersey P, Scolyer RA (2004) The history and future of melanoma staging. *J Surg Oncol* 86:224–235.
5. Thompson JF, Stretch JR, Uren RF, Ka VS, Scolyer RA (2004) Sentinel node biopsy for melanoma: Where have we been and where are we going? *Ann Surg Oncol* 11(Suppl):147S–151S.
6. Seftor EA, Seftor REB, Hendrix MJC (1990) Selection of invasive and metastatic subpopulations from a heterogeneous human melanoma cell line. *BioTechniques* 9:324–331.
7. Hendrix MJC, Seftor EA, ChuYW, Trevor KT, Seftor REB (1996) Role of intermediate filaments in migration, invasion, and metastasis. *Cancer Metastasis Rev* 15:507–525.
8. Hendrix MJ, et al. (1992) Coexpression of vimentin and keratins by human melanoma tumor cells: Correlation with invasive and metastatic potential. *J Natl Cancer Inst* 84:165–174.
9. Kozlowski JM, Hart IR, Fidler IJ, Hanna N (1984) A human melanoma line heterogeneous with respect to metastatic capacity in athymic nude mice. *J Natl Cancer Inst* 72:913–917.
10. Nagashima T, et al. (2002) Dynamic-enhanced MRI predicts metastatic potential of invasive ductal breast cancer. *Breast Cancer* 9:226–230.
11. Duvvuri U, et al. (2001) Water magnetic relaxation dispersion in biological systems: The contribution of proton exchange and implications for the noninvasive detection of cartilage degradation. *Proc Natl Acad Sci USA* 98:12479–12484.
12. Grohn OHJ, et al. (2000) Early detection of irreversible cerebral ischemia in the rat using dispersion of the magnetic resonance imaging relaxation time, $T_{1\rho}$. *J Cereb Blood Flow Metab* 20:1457–1466.
13. Kettunen MI, Brindle KM (2005) Apoptosis detection using magnetic resonance imaging and spectroscopy. *Prog Nucl Magn Reson Spectrosc* 47:175–185.
14. Kettunen MI, Grohn OHJ, Penttonen M, Kauppinen RA (2001) Cerebral $T_{1\rho}$ relaxation time increases immediately upon global ischemia in the rat independently of blood glucose and anoxic depolarization. *Magn Reson Med* 46:565–572.
15. Kettunen MI, Grohn OHJ, Silvennoinen MJ, Penttonen M, Kauppinen RA (2002) Effects of intracellular pH, blood, and tissue oxygen tension on $T_{1\rho}$ relaxation in rat brain. *Magn Reson Med* 48:470–477.
16. Quistorff B, Haselgrove JC, Chance B (1985) High-resolution readout of 3D metabolic organ structure: An automated, low-temperature redox ratio-scanning instrument. *Anal Biochem* 148:389–400.
17. Li LZ, et al. (2007) Predicting melanoma metastatic potential by optical and magnetic resonance imaging. *Oxygen Transport to Tissue XXVIII*, eds Maguire DJ, Bruley DF, Harrison DK (Springer, New York), Vol 599, pp 67–78.
18. Xu HN, et al. (2009) Histological basis of MR/optical imaging of human melanoma mouse xenografts spanning a range of metastatic potentials. *Oxygen Transport to Tissue XXX*, eds Liss P, Hansell P, Bruley DF, Harrison DK (Springer, New York), Vol 645, pp 247–253.
19. Zhou R, Pickup S, Yankeelov TE, Springer CS, Glickson JD (2004) Simultaneous measurement of arterial input function and tumor pharmacokinetics in mice by dynamic contrast enhanced imaging: Effects of transcytolemmal water exchange. *Magn Reson Med* 52:248–257.
20. Pickup S, Zhou R, Glickson J (2003) MRI estimation of the arterial input function in mice. *Acad Radiol* 10:963–968.
21. Yankeelov TE, Luci JJ, DeBusk LM, Lin PC, Gore JC (2008) Incorporating the effects of transcytolemmal water exchange in a reference region model for DCE-MRI analysis: Theory, simulations, and experimental results. *Magn Reson Med* 59:326–335.
22. Yankeelov TE, et al. (2005) Evidence for shutter-speed variation in CR bolus-tracking studies of human pathology. *NMR Biomed* 18:173–185.
23. Yankeelov TE, Rooney WD, Li X, Springer CS, Jr (2003) Variation of the relaxographic ''shutter-speed'' for transcytolemmal water exchange affects the CR bolus-tracking curve shape. *Magn Reson Med* 50:1151–1169.
24. Kim S, et al. (2007) Transcytolemmal water exchange in pharmacokinetic analysis of dynamic contrast-enhanced MRI data in squamous cell carcinoma of the head and neck. *J Magn Reson Imaging* 26:1607–1617.
25. Li X, et al. (2005) Shutter-speed analysis of contrast reagent bolus-tracking data: Preliminary observations in benign and malignant breast disease. *Magn Reson Med* 53:724–729.
26. Tofts PS, Beerkowitz B, Schnall MD (1995) Quantitative analysis of dynamic Gd-DTPA enhancement in breast tumors using a permeability model. *Magn Reson Med* 33:564–568.
27. Tofts PS, et al. (1999) Estimating kinetic parameters from dynamic contrast-enhanced T_1-weighted MRI of a diffusable tracer: Standardized quantities and symbols. *J Magn Reson Imaging* 10:223–232.
28. Makela HI, Grohn OHJ, Kettunen MI, Kauppinen RA (2001) Proton exchange as a relaxation mechanism for T_1 in the rotating frame in native and immobilized protein solutions. *Biochem Biophys Res Commun* 289:813–818.
29. Rommel E, Kimmich R (1989) $T_{1\rho}$ dispersion imaging and volume-selective $T_{1\rho}$ dispersion weighted Nmr spectroscopy. *Magn Reson Med* 12:390–399.
30. Chance B, Schoener B, Oshino R, Itshak F, Nakase Y (1979) Oxidation-reduction ratio studies of mitochondria in freeze-trapped samples. NADH and flavoprotein fluorescence signals. *J Biol Chem* 254:4764–4771.
31. Rofstad EK (2000) Microenvironment-induced cancer metastasis. *Int J Radiat Biol* 76:589–605.
32. Subarsky P, Hill RP (2003) The hypoxic tumor microenvironment and metastatic progression. *Clin Exp Metastasis* 20:237–250.
33. Gillies RJ, Raghunand N, Karczmar GS, Bhujwalla ZM (2002) MRI of the tumor microenvironment. *J Magn Reson Imaging* 16:430–450.
34. Vaupel P, Mayer A (2007) Hypoxia in cancer: Significance and impact on clinical outcome. *Cancer Metastasis Rev* 26:225–239.
35. Dewhirst MW, et al. (2005) Relation between pO2, 31P magnetic resonance spectroscopy parameters and treatment outcome in patients with high-grade soft tissue sarcomas treated with thermoradiotherapy. *Int J Radiat Oncol Biol Phys* 61:480–491.
36. Cavalli LR, Liang BC (1998) Mutagenesis, tumorigenicity, and apoptosis: Are the mitochondria involved? *Mutat Res* 398:19–26.
37. Modica-Napolitano JS, Singh KK (2004) Mitochondrial dysfunction in cancer. *Mitochondrion* 4:755–762.
38. Chance B, Williams GR (1955) A method for the localization of sites for oxidative phosphorylation. *Nature* 176:250–254.
39. Chance B, Baltscheffsky H (1958) Respiratory enzymes in oxidative phosphorylation. *J Biol Chem* 233:736–739.
40. Zhang Q, et al. (2006) Redox sensor CtBP mediates hypoxia-induced tumor cell migration. *Proc Natl Acad Sci USA* 103:9029–9033.
41. Bristow RG, Hill RP (2008) Hypoxia, DNA repair, and genetic instability. *Nat Rev Cancer* 8:180–192.
42. Gatenby RA, Gawlinski ET, Gmitro AF, Kaylor B, Gillies RJ (2006) Acid-mediated tumor invasion: A multidisciplinary study. *Cancer Res* 66:5216–5223.
43. Welch DR, et al. (1991) Characterization of a highly invasive and spontaneously metastatic human malignant melanoma cell line. *Int J Cancer* 47:227–237.
44. Borthakur A, et al. (2004) In vivo measurement of $T_{1\rho}$ dispersion in the human brain at 1.5 tesla. *J Magn Reson Imaging* 19:403–409.
45. Wheaton AJ, et al. (2004) In vivo quantification of $T_{1\rho}$ using a multislice spin-lock pulse sequence. *Magn Reson Med* 52:1453–1458.